Lack of embryonic skeletal muscle in mice leads to abnormal mineral deposition and growth

Journal of Structural Biology 217 (2025) 108178

Contents lists available at ScienceDirect

Journal of Structural Biology

journal homepage: www.elsevier.com/locate/yjsbi

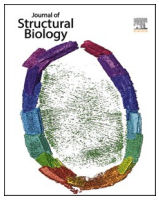

Research Article

Lack of embryonic skeletal muscle in mice leads to abnormal mineral deposition and growth

Isabella Silva Barreto [a,1,*], Marianne Liebi [b,c,d], Sophie Le Cann [a,e], Saima Ahmed [f], Leonard C. Nielsen [d], Tilman A. Grünewald [g,1], Hector Dejea [a,h], Viviane Lutz-Bueno [b], Niamh C. Nowlan [f,i], Hanna Isaksson [a]

[a] Department of Biomedical Engineering, Lund University, 223 62 Lund, Sweden
[b] Photon Science Division, Paul Scherrer Institut, 5232 Villigen PSI, Switzerland
[c] Institute of Materials, Ecole Polytechnique fédérale de Lausanne (EPFL), Lausanne, Switzerland
[d] Department of Physics, Chalmers University of Technology, Gothenburg, Sweden
[e] CNRS, Univ Paris Est Creteil, Univ Gustave Eiffel, UMR 8208, MSME, F-94010 Créteil, France
[f] Department of Bioengineering, Imperial College London, London, UK
[g] European Synchrotron Radiation Facility, Grenoble, France
[h] MAX IV Laboratory, Lund University, 224 84 Lund, Sweden
[i] School of Mechanical and Materials Engineering, University College Dublin, Dublin, Ireland

ARTICLE INFO

Keywords:
Mechanobiology
Hydroxyapatite
Zinc
Synchrotron imaging
X-ray scattering
X-ray fluorescence

ABSTRACT

Developing bones can be severely impaired by a range of disorders where muscular loading is abnormal. Recent work has indicated that the effects of absent skeletal muscle on bones are more severe early in development, with rudiment length and mineralization lengths being almost normal in muscle-less limbs just prior to birth. However, the impact of abnormal mechanical loading on the nanoscale structure and composition during prenatal mineralization remains unknown. In this exploratory study, we characterized the mineralization process of humeri from muscle-less limb embryonic mice using a multiscale approach by combining X-ray scattering and fluorescence with infrared and light microscopy to identify potential key aspects of interest for future in-depth investigations. Muscle-less humeri were characterized by initially less mineralized tissue to later catch up with controls, and exhibited continuous growth of mineral particles, which ultimately led to seemingly larger mineral particles than their controls at the end of development. Muscle-less limbs exhibited an abnormal pattern of mineralization, reflected by a more widespread distribution of zinc and homogenous distribution of hydroxyapatite compared to controls, which instead showed trabecular-like structures and zinc localized only to regions of ongoing mineralization. The decrease in collagen content in the hypertrophic zone due to resorption of the cartilage collagen matrix was less distinct in muscle-less limbs compared to controls. Surprisingly, the nanoscale orientation of the mineral particles was unaffected by the lack of skeletal muscle. The identified accelerated progression of ossification in muscle-less limbs at later prenatal stages provides a possible anatomical mechanism underlying their recovery in skeletal development.

1. Introduction

Bone is a dynamic tissue known to adapt to its local mechanical environment (Buckwalter et al., 1996; Frost, 2001). Its mechanical properties are dependent on the structure and properties on all hierarchical length scales (Reznikov et al., 2018). It has been shown that fetal immobilization can have dramatic effects on the developing skeleton (Nowlan et al., 2007; Sharir et al., 2011), with the mechanical environment affecting the mechanical competence of the mineralized tissues. For instance, multiple neuromuscular diseases which cause reduced or complete lack of fetal movement *in utero* lead to bones more prone to fracture in infants and children (Rodriguez et al., 1988; Ward et al., 2006).

The effects of reduced movement during embryonic bone

* Corresponding author.
E-mail address: isabella.silva_barreto@bme.lth.se (I. Silva Barreto).
[1] Present address: Aix Marseille Univ, CNRS, Centrale Med, Institut Fresnel, 13013 Marseille, France.

https://doi.org/10.1016/j.jsb.2025.108178
Received 22 October 2024; Received in revised form 7 February 2025; Accepted 11 February 2025
Available online 15 February 2025

development have been widely investigated in chick, mouse and zebrafish models (Nowlan et al., 2010). A common mouse model with muscle-less limbs is the $Pax3^{Spd/Spd}$ mutant, in which the lack of the transcription factor Pax3 prevents migration of muscle progenitor cells into the limb buds and consequently prevents the formation of skeletal muscles (Franz et al., 1993). The resulting morphology of the developing bones in this and other similar mice models is altered, where initially smaller mineralized regions, more circular cross-sectional areas and absence of or modified deltoid tuberosities are assumed to mainly be a consequence of reduced mechanical stimulation (Sharir et al., 2011; Nowlan et al., 2010; Gomez et al., 2007). Our group recently used synchrotron-based phase contrast microtomography to quantify the effects of absent skeletal muscle on the growth plate which governs the longitudinal bone growth, and bone mineralization patterns at the microstructural level (Pierantoni et al., 2021). When skeletal muscles were absent, a decreased volume of the mineralized region and an altered bone geometry were observed during the early stages of bone formation (Pierantoni et al., 2021; Sotiriou et al., 2022). Towards the end of embryonic development these alterations became less pronounced, indicating that the delayed mineralisation was partly recovered (Pierantoni et al., 2021; Sotiriou et al., 2022). During these early stages of bone formation, the density and size of the chondrocytes at the growth plate were also altered as a result of absent skeletal muscle. To improve our understanding of both healthy and pathological bone formation, elucidating the mechanobiological characteristics on all hierarchical length scales is crucial. However, our current knowledge on the effects of muscular loading on the mineralization process down towards the nanoscale is limited.

Long bones form through a combination of intramembranous (primary) and endochondral (secondary) ossification, where the former corresponds to direct apposition of disorganized woven bone by osteoblasts and the latter by a gradual replacement of a cartilaginous template (Olsen et al., 2000; Shapiro, 2008). In long bones, the primary ossification centre is formed in the midshaft of the bone through intramembranous ossification, followed by radial growth through intramembranous ossification of the bone collar and simultaneous longitudinal growth through endochondral ossification at the growth plate. As development progresses, the disorganized woven bone is remodelled into more well-aligned lamellar bone. Some aspects of the mineralization pathway are still being debated, such as the origin, delivery system and crystallization events of hydroxyapatite (HA, $Ca_5(PO_4)_3(OH)$) at the sites of mineralization. Once at the mineralization site, HA has been found to form small, spherulitic nanoscale mineral foci which then elongate their c-axis along the direction of the collagen fibril long axes and ultimately form cross-fibrillar mineral at the microscale (Buss et al., 2020). Recent evidence suggests that the formation of the nanoscale mineral spherulites starts in the interfibrillar compartment, to then spread across and into the fibrils (Macías-Sánchez et al., 2022). The stenciling principle introduced by Reznikov et al. (2020) describes a controlled and spatially precise mineralization process on the submicron scale of the skeletal regions to mechanically optimized locations and geometries, while at the same time keeping the neighbouring connective tissue soft.

To study the structure and composition of bone at the nanoscale, several high-resolution techniques can be used (Grünewald et al., 2024). Two-dimensional scattering techniques such as small- and wide-angle X-ray scattering (SAXS, WAXS) can estimate the size and orientation of the nanoscale HA mineral particles (Peyrin, 2009). SAXS and WAXS have been combined with conventional tomography (Wittig and Birkedal, 2022; Seidel et al., 2012), and more recently also with tensor tomography (SASTT, WASTT) (Liebi et al., 2015; 2018; Grünewald et al., 2020) to study bone around implants and biomaterials (Liebi et al., 2021; Casanova et al., 2023), mineral orientation and crystal structure (Mürer et al., 2021; Grünewald et al., 2023). Using scattering and electron microscopy techniques, mineral has been observed to reside in both intra- and extrafibrillar spaces, with up to 80 % of the mineral fraction being extrafibrillar (Reznikov et al., 2018; McNally et al., 2012; Schwarcz et al., 2014; Micheletti et al., 2023; Schwarcz et al., 2020), and a localized presence of misaligned extrafibrillar mineral particles with different lattice parameters has been found (Grünewald et al., 2020). The orientation of collagen fibres can be studied using polarized light, due to their intrinsic birefringence (Wolman and Kasten, 1986), and different types of polarized light microscopies (PLM) have been used on collagenous tissues such as bone (Bromage et al., 2003). To quantify the molecular and elemental composition of bone, spectroscopy techniques such as Fourier-transform infrared (FTIR) (Boskey and Camacho, 2007) and X-ray fluorescence (XRF) (Peyrin, 2009) are often used. The primary element of interest in mineralized tissues is Ca, which is the main component of HA. However, trace elements such as zinc (Zn) and iron (Fe) are also of interest (Percival, 1999). Zn has been shown to play a particularly important role during bone growth and bone mineralization (Ortega et al., 2004; Litchfield et al., 1998; Kim et al., 2009; Yamaguchi, 1998), presumably through its role as a co-factor for matrix metalloproteases (MMPs) and alkaline phosphatase (ALP). A recent *in vitro* study on bone mesenchymal stem cells also found that the biomineralization of the surrounding extracellular matrix (ECM) starts with Zn-HA nucleation within the cell (Procopio et al., 2019). While the techniques presented above have been used to study bone in its mature state or in *in vitro* systems, there are very few to no studies using these techniques on embryonic bone development and none have investigated the mechanobiological effects of reduced loading during this process.

To improve our limited understanding of how muscular loading affects bone formation at the nanoscale, this exploratory study aims to identify key factors of early embryonic long bone mineralization which could be impacted by the absence of skeletal muscle and thus should be the focus of future in-depth studies. This was achieved using a multimodal approach quantifying the effects of muscle loading over extensive areas, including the growth plate and bone collar, at multiple embryonic development stages and across several length scales. Specifically, we use a range of high-resolution scattering- and spectroscopy-based 2D and 3D imaging techniques (SASTT, SAXS, WAXS, PLM, FTIR and XRF) to study the maturation of the nanoscale structural organization in terms of both HA and collagen, as well as the distribution of trace elements, in $Pax3^{Spd/Spd}$ embryonic mice from start of mineralization to shortly before birth.

2. Materials and methods

2.1. Samples

This study used mice (n = 45, C57BL/6 strain) with and without skeletal muscles ($Pax3^{Spd/Spd}$). $Pax3^{Spd/Spd}$ (Splotch-delayed) muscle-less mice were interbred by spontaneous mating, where ~ 25 % of the embryos become muscle-less (Tajbakhsh et al., 1997). The absence of the transcription factor Pax3 prevents muscle progenitor cell migration into the limb buds, which in turn prevents the development of limb skeletal muscles (Franz and Kothary, 1993).

22 embryos with muscle-less forelimbs and 23 littermates with normal skeletal muscle (controls) were harvested at different developmental stages (Theiler stages TS) based on the Theiler morphological criteria (Theiler, 1989). Stages were included from the first sign of mineralization (TS23, approximately embryonic day 14.5) to shortly before birth (TS27, approximately embryonic day 18.5). The experimental protocol adhered to the ARRIVE guidelines and was conducted in accordance with European legislation (Directive 2010/63/EU), under project license number P39D18B9C. The humeri were carefully dissected, fixed and stored in 70 % ethanol until embedding. The humeri were divided into subgroups to be assessed with SASTT, SAXS, WAXS, XRF, FTIR and PLM (Table 1) each with field of view (FOV) and spatial resolution presented in Table 2. Some humeri were investigated with multiple techniques.

Table 1
The number of humeri evaluated per technique and development stage. The techniques used in this study to assess the structure and composition of humeri from muscle-less (M) forelimbs and their littermate controls (C) were: Fourier transform infra-red (FTIR) microspectroscopy and polarized light microscopy (PLM); small-angle X-ray scattering tensor tomography (SASTT); combined micrometre resolved small- and wide-angle x-ray scattering with x-ray fluorescence (μSAXS/WAXS/XRF); nanometre resolved x-ray fluorescence (nXRF).

Developmental stage	TS23		TS24		TS26		TS27	
Group	**C**	**M**	**C**	**M**	**C**	**M**	**C**	**M**
FTIR/PLM	N = 4	N = 4	N = 4	N = 4	N = 5	N = 4	N = 4	N = 4
SASTT	N = 1	N = 1	N = 1	N = 1	N = 1	N = 1	N = 1	N = 1
μSAXS/WAXS/XRF	–	–	N = 1	N = 1	–	–	N = 1	N = 1
nXRF	–	–	–	–	–	–	N = 1	N = 1

Table 2
Approximate field of view (FOV) and spatial resolution obtained per technique. Given the time constraints and limitations of each technique, the FOVs were adapted or multiple FOVs were acquired when necessary to fit as much of the regions of interest as possible. The regions of interest were the growth plate / mineralization front, which spans a few hundred μm in length (Pierantoni et al., 2021), and the bone collar, which spans a few tens of μm in thickness (Sharir et al., 2011).

	Pixel size (μm)	FOV (μm)
SASTT	25	500–1500 x 500–1500
FTIR	4.6	300 x 800
μSAXS/WAXS/XRF	2	500 x 500
PLM	0.5	1000 x 1000
nXRF	0.1	40 x 80–200

2.2. Synchrotron small-angle X-ray scattering tensor tomography (SASTT)

SASTT was performed on humeri from 8 forelimbs (Table 1) at the cSAXS beamline, Paul Scherrer Institute (PSI), Switzerland. Measurements were conducted over a FOV including at least one mineralization front of a growth plate and the bone collar to evaluate both new bone formation as well as a few days older tissue. Scans were acquired using a beam energy of 11.2 keV, step size of 25x25 μm^2, exposure time of 30 ms and a sample detector distance of 2.165 m. The samples were scanned with isotropic angular sampling in both rotation and tilt directions, acquiring 2D projections of scattering patterns at equally spaced rotations between 0° and 180° at 0° tilt and between 0° and 360° at 6 tilt angles, while ensuring equal angular sampling (Liebi et al., 2015; Liebi et al., 2018). No substantial effect of radiation was identified on the mineral structure, as the SAXS signal remained unchanged between the start and end of each measurement (Supporting Information, Methods S1 and Fig. S1).

All scattering patterns were integrated in two q-regions related to the scattering from the mineral particles (Fig. 2.A). To evaluate mineral particle orientation, the reciprocal space map in each voxel was reconstructed in the q-range 0.5–0.6 nm^{-1} (Fig. 2.A, green shaded area) using spherical integral geometric tensor tomography (SIGTT) (Nielsen et al., 2023) with the software package MUMOTT version 0.2 (Nielsen et al., 2023). To evaluate mineral particle thickness T, reconstruction using the zonal spherical harmonics tensor tomography (ZHTT) method (Liebi et al., 2015; 2018; 2021) was performed in 200 logarithmically spaced q-bins in the q-range 0.1–4 nm^{-1} (Fig. 2.A, red line) and fitted assuming a platelet shape (Turunen et al., 2014; Bünger et al., 2010), as previously described (Silva Barreto et al., 2020). For more information on the SASTT measurements and data analysis, see Supporting Information, Method S1 and Table S1.

2.3. Synchrotron scanning small-/wide-angle X-ray scattering (SAXS, WAXS) and X-ray fluorescence (XRF)

Simultaneous micrometre resolved SAXS, WAXS and XRF was performed on humeri from 4 forelimbs (Table 1) at the ID13 beamline, European Synchrotron Radiation Facility (ESRF), France. Measurements were conducted over a FOV including at least one mineralization front of a growth plate and the bone collar, using a beam energy of 13 keV, 50 ms exposure time, spot and step size of 2x2 μm^2. Diffraction patterns were collected using an Eiger 4 M X detector at a sample-detector distance of 93 mm and XRF spectra were collected using a single element Vortex EM detector (Hitachi High-Technologies Corp, US) at a sample-detector distance of 20 mm and at an angle of approximately 70° with respect

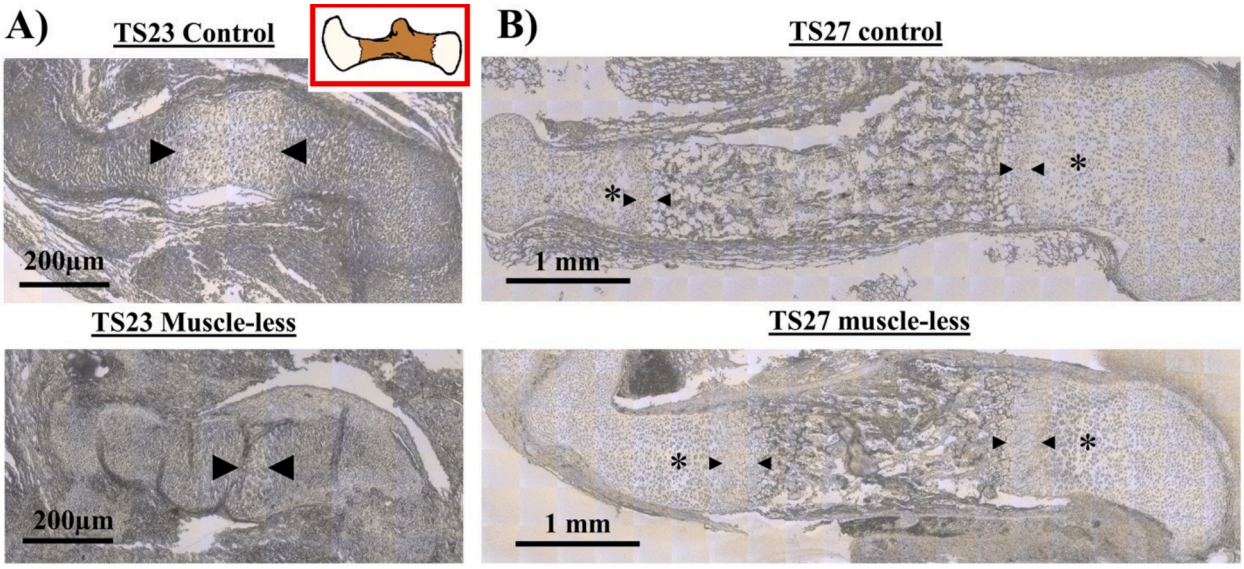

Fig. 1. Morphological representation of controls and muscle-less limb humeri. Representative microscope images of humeri from control and muscle-less limbs at TS23 (A) and TS27 (B). Sections from muscle-less humeri at TS23 exhibited sectioning artefacts such as folding, which did not occur in any of the control samples. The hypertrophic zones are indicated with black arrowheads (►◄) and the proliferative zone by an asterisk (*).

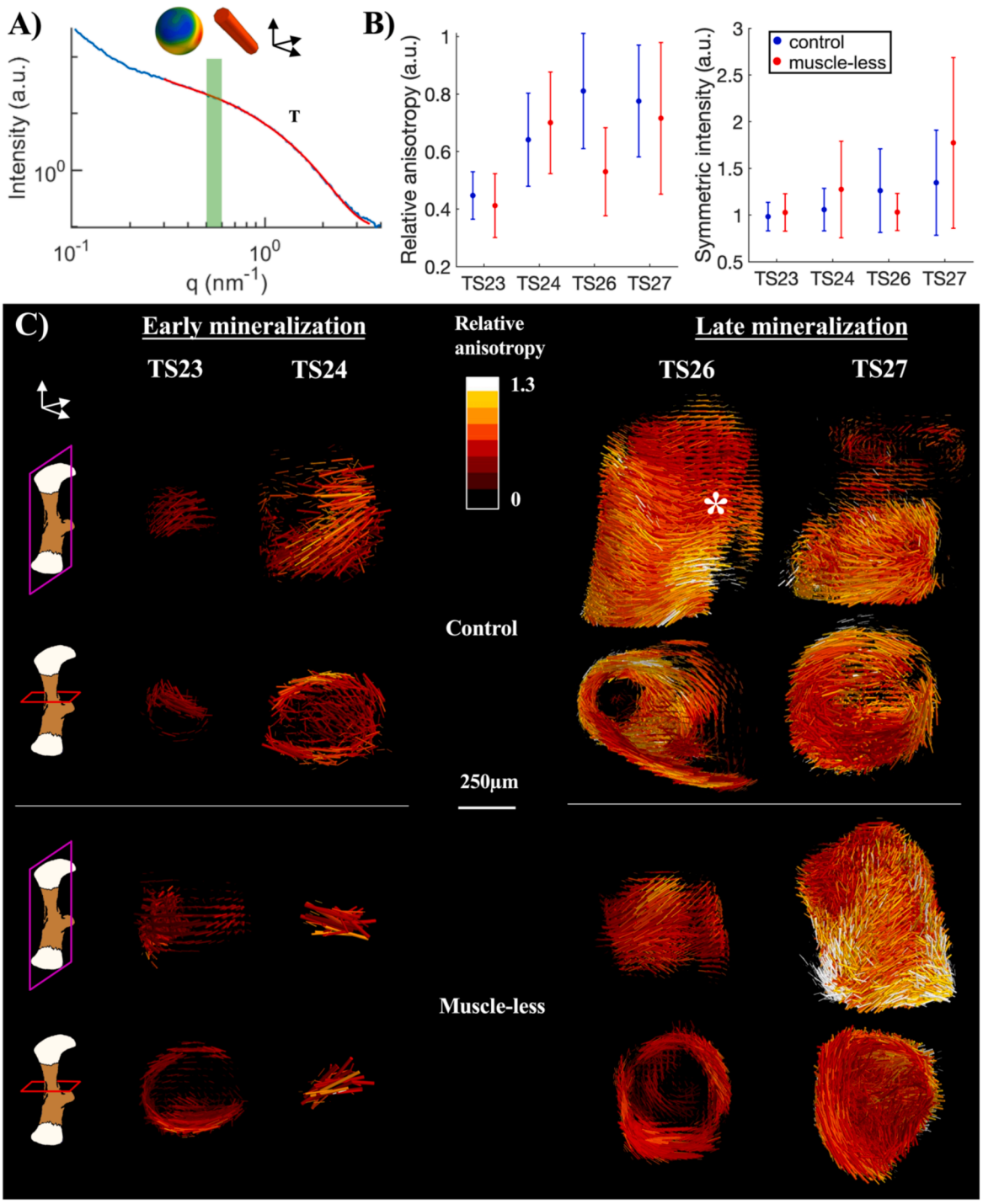

Fig. 2. 3D nanostructural orientation of mineralized tissue, based on SASTT. A) Radially integrated scattering intensity curve, showing the q-region used for orientational analysis with SIGTT (green shaded area), an example of a reconstructed reciprocal space map and the corresponding estimated nanoscale mineral particle orientation, as well as a fit of the I(q) curve for mineral particle thickness T (red line) after q-resolved ZHTT reconstruction. B) Average relative anisotropy and symmetric intensity of the mineral particles across all sample-related voxels. Error bars indicate the standard deviation within each sample. C) Glyph render at longitudinal (purple) and transversal (red) views of the mineralized humeri, reconstructed using SIGTT (band-limit $\ell \leq 6$), showing the main orientation of the nanoscale mineral particles (glyph direction), mean scattering intensity (glyph size) and relative anisotropy (color scale), respectively indicating the amount of crystalline mineral particles present and their degree of alignment. The deltoid tuberosity is visible in TSS26 control (asterisk). (For interpretation of the references to color in this figure legend, the reader is referred to the web version of this article.)

to the incident x-ray beam. The scattering patterns were analyzed using in-house codes in MATLAB (MathWorks Inc. US), following our previously described protocols (Silva Barreto et al., 2020) for mineral particle orientation, thickness T as well as the length L and width W of coherently scattering domains in the 002- and 310-direction (Fig. 3.A), respectively. The µXRF spectra were analyzed using the XRF analysis program PyMCA (Solé et al., 2007) for elemental intensities at each scanned point, following previously described protocols (Silva Barreto et al., 2020). Based on our previous studies (Dejea et al., 2023; Silva Barreto et al., 2020; Sharma et al., 2024), Ca and Zn were chosen for

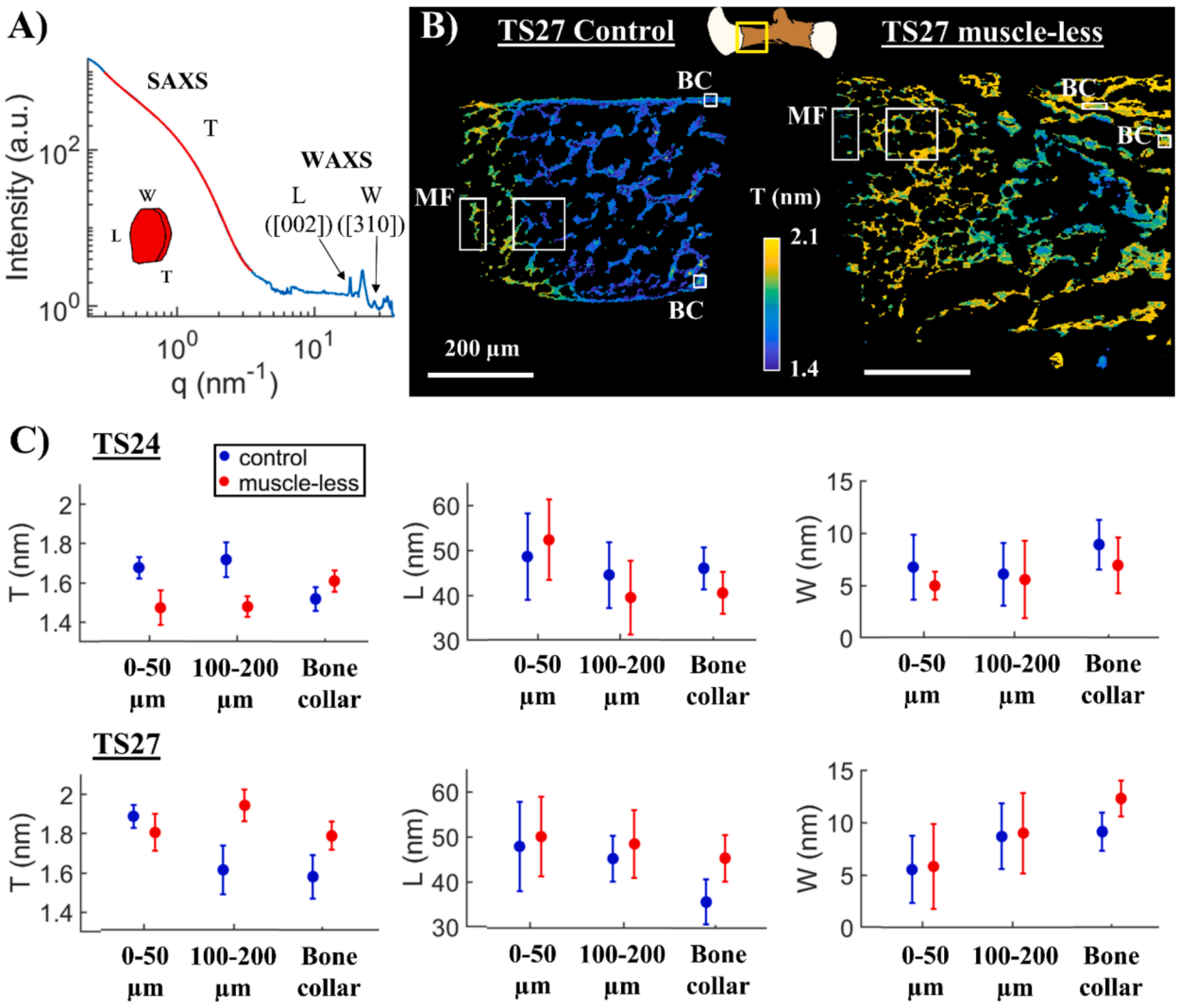

Fig. 3. HA mineral particle dimensions acquired by 2D SAXS and WAXS. A) Radially integrated scattering intensity curve, showing the q-regions of SAXS and WAXS, as well as the fit related to thickness (T, red line) and the peaks related to length (L) and width (W) of coherently scattering domains in the 002- and 310-direction, respectively. B) Spatial distribution maps of mineral thickness in the control and muscle-less humeri at TS27, showing the regions of interest which were further analyzed; mineralization front (MF) and bone collar (BC). C) Average mineral particle dimensions of all sample-related points (per sample) at the first 50 µm of the mineralization front, in a region 100–200 µm further into mineralization as well as two areas of approximately 20x20 $µm^2$ each within the bone collar. Error bars indicate the standard deviation within each area. (For interpretation of the references to color in this figure legend, the reader is referred to the web version of this article.)

more detailed micrometre resolved analysis (Fig. 5.A).

To gain more detailed information on the most active regions of mineralization, nanometre resolved XRF was performed at NanoMAX beamline, MAX IV, Sweden, on the two TS27 embryonic forelimbs imaged at ESRF. Measurements were conducted over smaller FOVs of the mineralization front at the growth plate, approximately 200 µm into mineralization and the bone collar, using a beam energy of 12 keV, 100 nm step size (~80 nm spot size) and 80 ms exposure time. The XRF spectra were collected using a single-element silicon drift detector (RaySpec, UK) coupled to an Xpress 3 pulse processor (Quantum Detectors, UK) at a sample-detector distance of approximately 25 mm and at an angle of 90° with respect to the incident x-ray beam. The sample was rotated 15° towards the XRF detector. The elemental concentrations at each scanned point were estimated in PyMCA (Solé et al., 2007) using a thin film standard (RF-C00, AXO Dresden GmbH, Germany), as previously described (Silva Barreto et al., 2020). Based on previous studies (Dejea et al., 2023; Silva Barreto et al., 2020; Sharma et al., 2024), Ca, Zn and Fe were chosen for more detailed analysis.

For detailed information on the SAXS, WAXS and XRF measurements and data analysis, see Supporting Information, Method S2.

2.4. Polarized light microscopy (PLM)

To evaluate collagen fiber orientation, PLM measurements were conducted on humeri from 33 forelimbs (Table 1) using a birefringence imaging microscope (Exicor Birefringence Microimager, Hinds Instruments, Inc., OR, USA). Images were captured with a FOV including the whole humerus using a CCD camera and a 10X objective, resulting in a spatial resolution of 0.5 µm. A stroboscopic LED of wavelength 475 nm was used to calculate the Mueller matrix components in order to quantify and retrieve maps of the collagen fibers angle of their optical fast axis and retardance (phase shift between transmitted waves, related to alignment) (Han and Chao, 2006; Nichols et al., 2014). For detailed information on the PLM measurements, see Supporting Information, Method S3.

2.5. Fourier transform infra-red microspectroscopy (FTIR)

To evaluate the molecular composition, FTIR measurements were conducted on the same sections of the 33 humeri as measured with PLM. Measurements were conducted in transmission over FOVs of the growth plate (including the mineralization front) and the bone collar using a Bruker Hyperion 3000 IR microscope (Bruker Corp, USA) with a 64 x 64 focal plane array detector. Measurements were acquired with a spatial resolution of 2.3 μm, spectral resolution of 4 cm^{-1} and 64 repeated scans. Mineral, collagen (matrix) and mineral to matrix ratio (M:M) were estimated from the spectra (Fig. 4.A), following previously described protocols (Silva Barreto et al., 2020). For detailed information on the FTIR measurements and data analysis, see Supporting Information, Method S4.

2.6. Statistics

For all data acquired in this study, mean and standard deviation were calculated. For the FTIR and PLM data, Wilcoxon rank sum test was performed to test for statistically significant differences between muscle-less and control humeri at each development stage. For the SASTT, SAXS, WAXS and XRF data, the low sample numbers make statistical testing unfeasible. Instead, we focus on descriptive findings that were similar across several developmental stages.

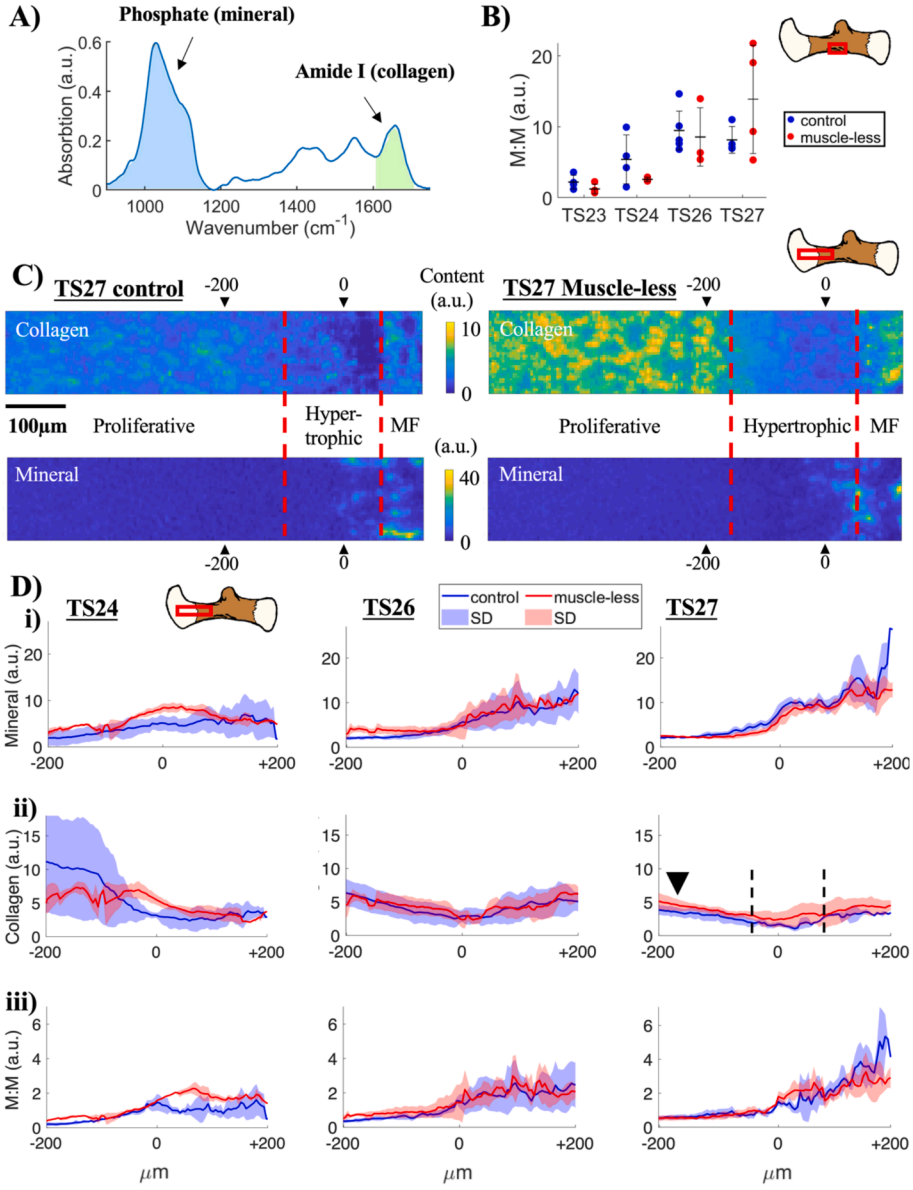

Fig. 4. Molecular composition at the growth plate and bone collar acquired by FTIR. A) Representative FTIR spectrum from one pixel within the bone collar, indicating the peaks related to phosphate (mineral) and amide I (collagen, matrix) content. B) Average mineral to matrix ratio (M:M) ratio in the bone collar, within two areas in each sample of approximately 40x40 $μm^2$. C) Representative collagen and mineral maps from growth plates at TS27, indicating the proliferative and hypertrophic zone, as well as the mineralization front (MF). The maps were aligned to the onset of mineralization (0) and longitudinally averaged from 200 μm into the unmineralized cartilage (−200) to 200 μm into the mineralized bone. D) Average longitudinal profiles of mineral (i) and collagen (ii) content, as well as M:M ratio (iii), across the growth plates and mineralization front. The profiles were aligned at M:M ratio of 1.5, which was found to be the best match of the onset of mineralization for all samples, stages and groups. The increased collagen content in the proliferative zone of the TS27 muscle-less humeri (arrowhead) and lack of synchronized decrease in collagen within the hypertrophic zone are indicated (dashed lines).

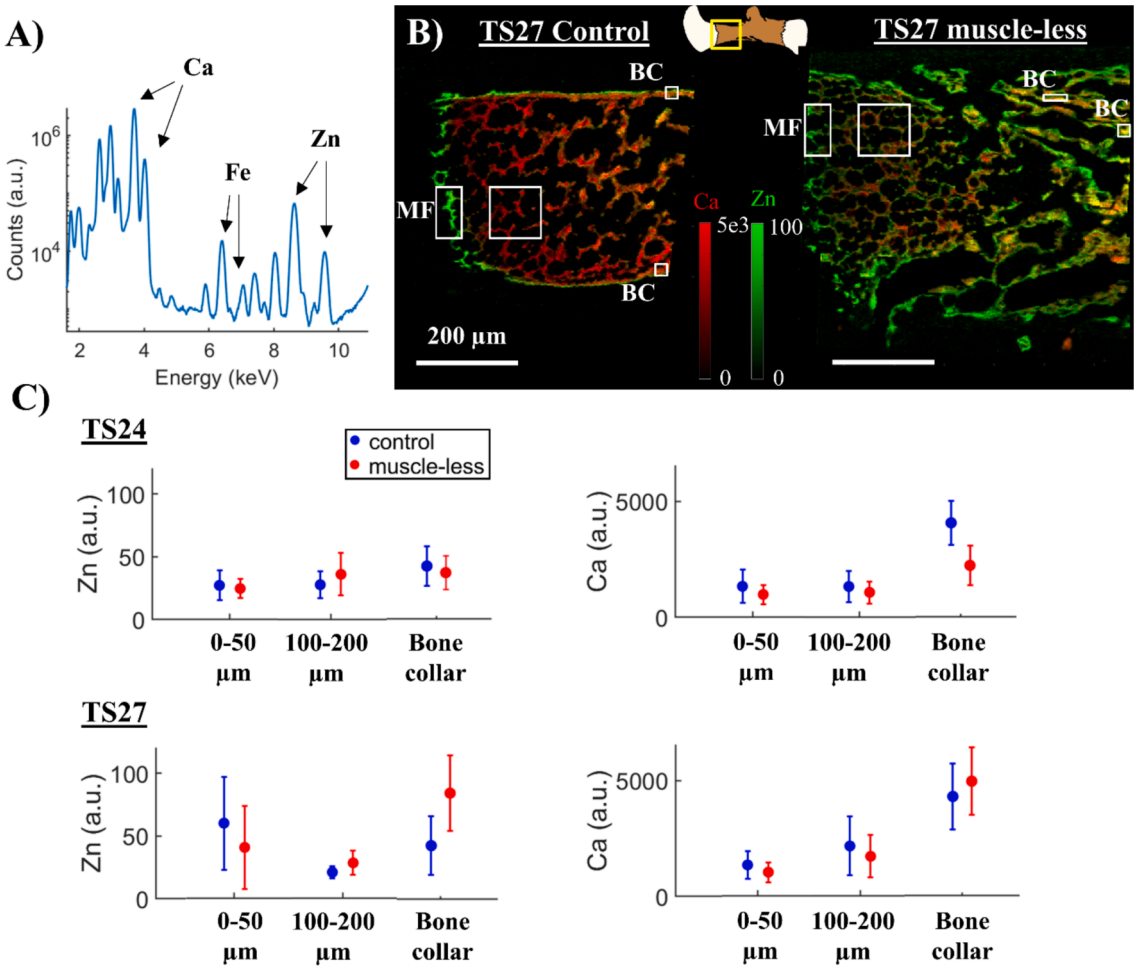

Fig. 5. Spatial distributions of Ca and Zn content acquired by micrometre resolved XRF. A) Representative XRF spectrum from one pixel, indicating the peaks related to Ca and Zn (further analyzed by µXRF) content as well as Fe (further analyzed by nXRF). B) Combined spatial distribution maps of Ca (red) and Zn (green) of one control humeri and one muscle-less humeri at TS27; overlap of the two elements is yellow. White boxes represent the further analyzed regions of interest: first 50 µm of mineralization front (MF) and 100–200 µm into mineralization, as well as the bone collar (BC). C) Averaged Zn and Ca intensities within the regions of interest at TS24 and TS27, the error bars represent the standard deviation within the areas. (For interpretation of the references to color in this figure legend, the reader is referred to the web version of this article.)

3. Results

3.1. Morphology

Microscopy images taken during the FTIR measurements showed a morphology of humeri from muscle-less limbs with less humeral features compared to controls (Fig. 1). This confirms data presented in earlier studies using histological methods of this and similar animal models (Sharir et al., 2011; Nowlan et al., 2010; Gomez et al., 2007; Pierantoni et al., 2021; Sotiriou et al., 2022; Ahmed et al., 2023). While the size of the mineralized region in muscle-less humeri were similar to their controls at TS27, alterations in the length of their hypertrophic zones were apparent (Fig. 1.B).

3.2. 3D structural characterization

The 3D SASTT characterization of the nanoscale mineral particle orientation in the mineralized regions revealed that the average amount of crystalline mineral particles present (indicated by mean scattering intensity) in the muscle-less humeri and their alignment (relative anisotropy) were similar to controls during early mineralization (TS23-TS24, Fig. 2.B-C). The size of the mineralized region of the muscle-less humeri remained small until TS27 (Fig. 2.C), at which stage both the size of the mineralized regions and the alignment of the mineral particles were similar to controls (Fig. 2.B-C). Both groups exhibited similar orientation of the nanoscale mineral particles across development (glyph orientation, Fig. 2.C). In both groups, the mineral particles exhibited a low degree of alignment with the long bone axis (Supporting Information Video S1 and Fig. S2). Instead, they were more diagonally oriented around the shaft at all development stages, as well as along structural features such as the deltoid tuberosity (TS26 control, asterisk, Fig. 2.C). At TS27 this orientation around the shaft was less clear and some regions of the bone collar showed a higher alignment with the long bone axis in both groups (Supporting Information Fig. S2, asterisks).

The 3D SASTT characterization of the nanoscale mineral particle thickness revealed that during early mineralization (TS23-TS24), the humeri from muscle-less forelimbs had thinner mineral particles than controls (Supporting Information Fig. S3, muscle-less: 1.45 ± 0.16 nm, controls: 1.60 ± 0.12 nm). However, by late mineralization (TS26-TS27) the particle thickness was similar (muscle-less: 1.66 ± 0.13 nm, controls: 1.66 ± 0.13 nm). Despite the similar particle thickness at TS26 and TS27, muscle-less humeri showed a more spatially homogenous distribution of thicker particles across the rudiment compared to controls, which instead exhibited more structural heterogeneity with thicker particles at the mineralization front as well as close to the forming bone collar (Supporting Information Fig. S3, arrowheads), with a sharp

difference between these and their lower values at the center of the bone (Supporting Information Fig. S3, star).

3.3. 2D structural characterization

The 2D SAXS and WAXS characterization of the nanoscale mineral particle dimensions retrieved from the fits of the mineral shoulder, [002]- and [310] peaks (Fig. 3.A) showed that the mineral particles of the humeri from muscle-less forelimbs exhibited a more widespread spatial distribution of thicker particles at TS27 compared to controls (Fig. 3.B, Supporting Information Fig. S4). As opposed to controls, muscle-less humeri did not show a clear localization of thicker, longer and narrower mineral particles in less mature regions such as the mineralization front, compared to their bone collars (Fig. 3.C, Supporting Information Fig. S4) (Silva Barreto et al., 2020). Additionally, the muscle-less humeri exhibited an increasing trend between TS24 and TS27 within the bone collar in all mineral particle dimensions (Fig. 3.C, Supporting Information Fig. S4), with the muscle-less humerus at TS27 having on average larger particles in the bone collar compared to the control.

In humeri from both control and muscle-less forelimbs at all stages studied by 2D SAXS and PLM, the collagen and mineral particles in the bone collar were aligned with the long bone axis (Supporting Information Fig. S5). At TS27, internal collagen and mineral were also aligned with the main directions of their internal trabecular-like structures. Initially, lack of muscle was associated with a lower degree of mineral particle orientation within the bone collar (Supporting Information Fig. S5.B) but did not appear to affect collagen alignment (Supporting Information Fig. S5.A). As development progressed, alignment increased in both groups and the muscle-less humeri caught up in mineral degree of orientation by TS27.

3.4. Molecular characterization

The 2D FTIR characterization of the phosphate (mineral) and collagen (matrix) content (Fig. 4.A) revealed that the bone collar of muscle-less humeri at TS23 and TS24 were in the lower range of mineral to matrix ratios (M:M) compared to controls (Fig. 4.B). At the TS26 and TS27, however, the M:M ratio was similar between the two groups, but the muscle-less humeri exhibited a larger variation. Due to folding artefacts in the sections of the muscle-less humeri at TS23 (Fig. 1.A), we focused the profile analysis of the growth plate on the other stages. At TS27, the larger hypertrophic zones of the muscle-less humeri were accompanied by extended regions of the characteristic decrease in collagen content related to the degradation of the cartilage template prior to the mineralization front (Fig. 4.C, Fig. 4.D, ii dashed lines). In general, the collagen content was slightly elevated in muscle-less humeri at TS27, in particular within the proliferative zone (Fig. 4.C, Fig. 4.D, ii arrowhead). However, the typical decrease in collagen content within the hypertrophic zone was less pronounced in the muscle-less humeri compared to controls, as well as less spatially synchronized between samples and development stages, as indicated by their flatter average profiles (Fig. 4.D, ii). Especially at TS27, at which stage the decrease in collagen was most clear and synchronized in the controls, the lack of synchronization in the muscle-less humeri were demonstrated by a larger standard deviation within this region.

The effects of absent skeletal muscle on the growth plate and mineralization front were most pronounced at TS24, with clear differences in profiles (Fig. 4.D). The pattern of mineral development in muscle-less humeri was also altered at the mineralization front of the growth plate, resulting in an unchanged M:M ratio (~2 a.u.) across development, as opposed to controls in which it increased (Fig. 4.D).

3.5. Elemental characterization

Micrometre resolved XRF characterization of the elemental distributions of Ca and Zn revealed that the Zn distribution was spatially similarly at TS24 in control and muscle-less humeri (Fig. 5 and Supporting Information Fig. S6). At TS27, however, the muscle-less humerus showed a homogenous spatial distribution of Zn almost everywhere in the ECM, while in the control Zn was primarily localized to the mineralization front and outlining the bone collar (Fig. 5.B). In the control, the highest Zn content was found within the first 50 μm of the mineralization front, followed by a lower Zn content 100–200 μm into mineralization (Fig. 5.C). In the muscle-less humerus, the Zn content was also high in the first 50 μm of the mineralized front but remained elevated further into mineralization as well as on average within the bone collar (Fig. 5.D). Ca remained low at the mineralization front throughout development in both groups (Fig. 5.C), with higher Ca content in the bone collar. At TS24, microscale Ca appeared lower in the bone collar of the muscle-less humerus, but at TS27 it had reached similar values as the control (Fig. 5.C).

Nanometre resolved XRF characterization of the elemental distributions of Ca, Zn and Fe revealed that Ca was localized into clusters in the ECM of the TS27 control and Zn together with Fe were mainly present at the edges of these (Fig. 6.A-B). In the muscle-less TS27, however, both Ca and Zn had a more homogenous distribution, similarly as observed with micrometre resolved XRF (Fig. 5.B). In muscle-les humeri, Zn increased further into the mineralized structures and only Fe had an increased localization at their edges compared to their core (Fig. 6.B). A lower local nanoscale Ca and a higher Zn concentration was observed both at the mineralization front and in the bone collar of the muscle-less humerus compared to the control (Fig. 6.C). In the bone collar of the control, there was almost no Zn present.

4. Discussion

In this study, we assessed how lack of muscles affects the early mineralization process in humeri from embryonic mice using a wide range of novel high-resolution tissue characterization techniques. This enabled us to identify changes in the mineral nanostructure, as well as the molecular and elemental distribution with high spatial resolution. To our knowledge, this study is the first to investigate the effect of lack of embryonic skeletal muscles on bone formation using synchrotron X-ray scattering and fluorescence, as well as infrared and polarized light microscopy. This exploratory multimodal approach provides a step towards a better understanding of the mechanisms involved during embryonic mineralization, highlighting potential aspects that needs further focus in future studies. Interestingly, the findings of this study indicate that lack of skeletal muscles could result in an abnormal mineral particle deposition and growth, with the muscle-less humeri exhibiting seemingly larger mineral particles just prior to birth. This could possibly be due to a more widespread distribution of Zn, indicating more active but undirected ongoing mineralization throughout the entire muscle-less humeri. Keeping in mind that these findings need to be confirmed on a larger sample set, the implication of each identified potential key aspect is discussed below.

4.1. Lack of skeletal muscles might lead to a delayed and dysregulated mineral deposition and growth

During early mineralization, muscle-less humeri were smaller with lower Ca content compared to controls (Figs. 2, 5). By TS27, however, both the size of the mineralized region and overall Ca had increased to similar levels as controls. Additionally, while the humeri of the controls quickly attained a high level of mineralization, muscle-less humeri exhibited a more spread out, but steady increase throughout the investigated development stages which ultimately reached similar levels as controls (Fig. 4.B). These results indicate that the recovery in size is a result from an upregulated mineral deposition in muscle-less humeri some time between TS24 and TS27, at which point they seemingly deposit and form mineral substantially faster than controls. Their more

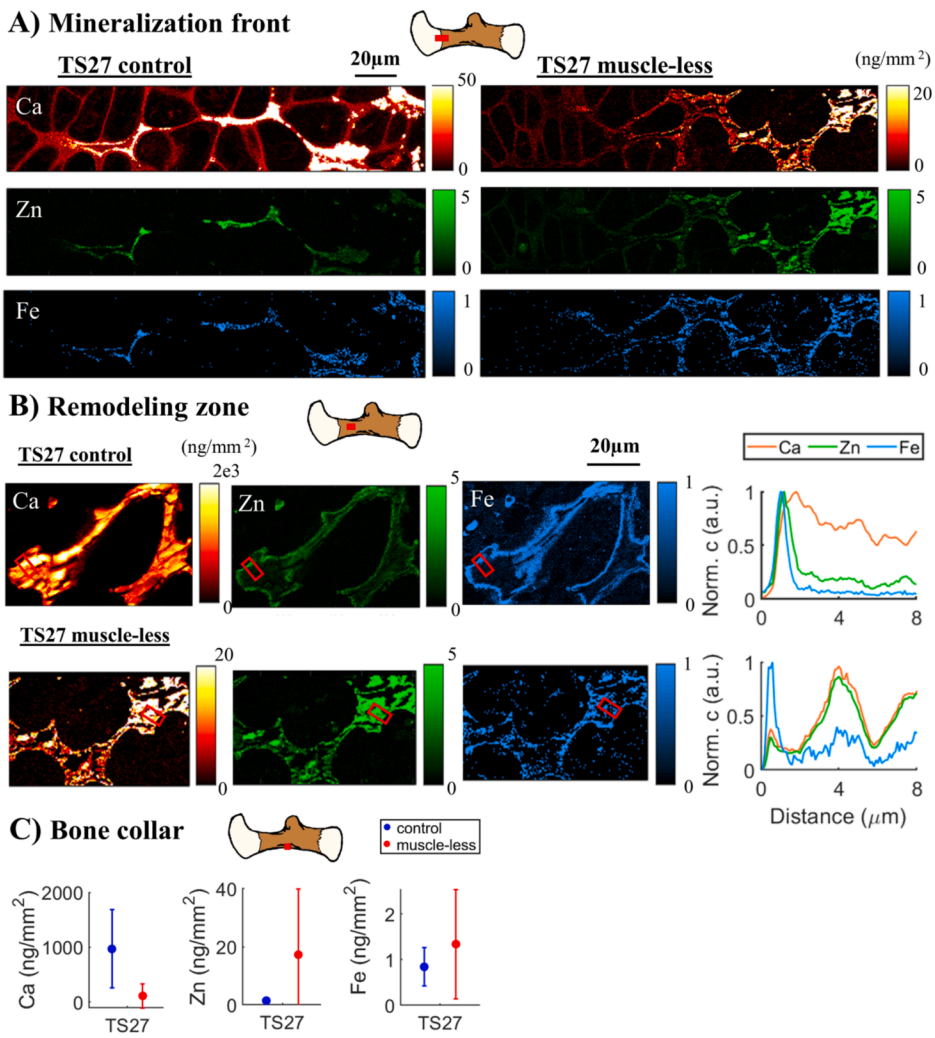

Fig. 6. Spatial distributions of Ca, Zn and Fe content acquired by nanometre resolved XRF. Approximate position of the different regions is indicated by the red rectangles on the schematics, enlarged for visualization purposes. A) Spatial concentration maps at the mineralization front in one control and one muscle-less TS27. All maps are saturated to highlight the internal structure. B) Spatial concentration maps of mineralized structures in the remodelling zone, approximately 200 µm into mineralization. Average profiles across the edge and into a mineralized structure (across regions indicated by red boxes on the elemental maps), normalized to the individual maximum values to highlight the trends in concentration. C) Average concentrations in the bone collar, within two areas in each sample of approximately 20x20 µm^2. (For interpretation of the references to color in this figure legend, the reader is referred to the web version of this article.)

homogenously widespread spatial distribution of large mineral particles and their increase in particle size differed from controls (Fig. 3). As previously discussed (Silva Barreto et al., 2020), during normal development the particles instead become thinner and shorter between TS24 and TS27, with a clear localization of less elongated, bulkier particles at the mineralization front. That the larger mineral particles of muscle-less humeri were not accompanied by an increase in Ca could indicate that 1) instead of forming more particles, the deposited mineral aids the growth of those already present. As recent evidence suggests mineral formation to start outside of the fibrils (Macías-Sánchez et al., 2022) and a difference in lattice parameters between intra- and extrafibrillar particles (Grünewald et al., 2020), it could also indicate that 2) their ratio between intra- and extrafibrillar mineral are altered and that there is a potentially higher presence of newly formed mineral. Additionally, differently shaped particles could also cause an alteration in thickness and thus the results could also indicate that 3) the mineral particles are differently organized, with different packing degrees and shape. While this study cannot confirm these hypotheses, it is highly likely that not only one of these processes occur, but rather that the observed more widespread distribution of apparently larger particles is due to a combination of them.

4.2. Skeletal muscles might not govern nanoscale orientation during embryonic long bone development

It is well accepted that the nanoscale collagen and mineral in adult bone organizes according to the directions of the loads it is subjected to; where different skeletal muscle attachments are responsible for the specialized macroscopic shape and the predominant orientation in the shaft of long bones is parallel to their long axis (Buckwalter et al., 1996; Frost, 2001). Despite this, we did not find any effect of skeletal muscles on the nanoscale orientation during embryonic bone development at the probed spatial resolution (Fig. 2, Supporting Information Fig. S2). The nanoscale structure in both groups became increasingly more aligned with age, with both collagen and mineral following the direction of the structural features (Fig. 2, Supporting Information Fig. S5). This indicates that 1) lack of skeletal muscles does not override the genetic template for the structural organization of the mineralized fibrils, 2) there is another key player than solely skeletal muscles which influence their organization and 3) woven bone is not fully randomly organized, as the initially laid down woven bone has most likely not yet been remodelled into lamellar bone (the timespan from start of mineralization to the latest development stage prior to birth is about 4 days).

However, an increase in alignment could be seen internally in both groups, with the structures at the mineralization front being less aligned compared to more mature tissue such as the bone collar. This also indicates that there may still be some minor loading induced on the bones from the surrounding environment even when skeletal muscles are absent (Nowlan et al., 2012), which potentially is enough to guide the developing bones at this stage.

Surprisingly, the SASTT characterization revealed that the nanostructure was not oriented parallel to the long bone axis (Fig. 2) as observed in the 2D PLM and SAXS measurements (Supporting Information Fig. S5) and previously reported for adult bone (Buckwalter et al., 1996; Frost, 2001), but instead around the shaft and following structural features such as the deltoid tuberosity (Supporting Information Video S1 and Fig. S3). While not directly comparable, a similar difference in the alignment between new and older bone has also been observed in 2-month old infants (Roschger et al., 2001). Additionally, a recent study investigating bone fracture healing with SASTT (Casanova et al., 2023) found that the nanostructure of the uninjured cortical (lamellar) bone to be longitudinally oriented, while the newly regenerated (woven) bone exhibited a more twisted orientation similar to what we found in the embryonic bones. This is also supported by recent findings where 3D surface geometry was studied *in vitro*. Substrate curvature was found to be important for tissue formation, which may explain the developing twisted-plywood-like structures in tissues (Schamberger et al., 2024) Most studies of postnatal and adult bone have so far used 2D techniques to assess nanoscale orientation, but these orientational differences between woven and lamellar bone, as well as the observed discrepancies between 2D and 3D measurements in this study, suggest that the current notion of the nanoscale mineral and collagen being aligned with the long bone axis might be an oversimplification. Additionally, it highlight the need for further 3D investigations and raises the question if the orientation of bone nanoscale structure may be more complex than previously reported.

4.3. Refined bone modelling could be inhibited by lack of skeletal muscle

In the controls, the mineralization front exhibited highly localized clusters of Ca in the ECM, and the trabecular-like internal structures deeper into mineralization were outlined by Zn and Fe (Fig. 6). In the muscle-less humeri, however, Ca was instead distributed homogenously within the ECM. Fe was still localized to the edges of their internal structures, but also remained more elevated inside them while following the changes in Ca. Literature regarding the role of Fe in bone mineralization is sparse, but some *in vitro* studies have found that Fe deficiency affects bone fragility, architecture, turnover, cell differentiation and activity, matrix formation and mineralization (Balogh et al., 2018). In muscle-less humeri, Zn was not localized at the edges of the internal structures, but instead increased with distance into them. Zn has a stimulatory effect on bone formation (Yamaguchi, 1998) and Zn deficiency has been found to affect bone length and morphology of the growth plate (Kim et al., 2009). Zn is a co-factor to many MMPs crucial to bone mineralization (Ortega et al., 2004; Litchfield et al., 1998) as well as expressed by bone-lining cells responsible for modelling the internal tissue into trabeculae (Ortega et al., 2004). Additionally, Zn can substitute Ca in HA, which has been shown to occur during early stages of *in vitro* mineralization in bone mesenchymal stem cells (Procopio et al., 2019). While the data of this study cannot reveal in which form Zn and Fe are present, we and others have previously reported a clear localization of Zn during normal bone development to the regions where new mineral is being deposited (Silva Barreto et al., 2020; Brister et al., 2020), outlining heterotopic ossifications in healing tendons (Sharma et al., 2024), as well as in proximity to MMP13 during bone fracture healing (Dejea et al., 2023).

The specific localization of Zn in controls combined with their more specialized microstructure (Fig. 5) and localized differences in mineral particle size (Fig. 3) suggest that normal humeri undergo refined microstructural modelling as their tissue matures. The more homogenous distribution of Zn, Ca and larger mineral particles in muscle-less humeri instead indicate that while they ultimately mineralize to a similar extent, they do not undergo as controlled ossification as during normal development. Additionally, the lack of a synchronized reduction in collagen content within the hypertrophic zones of muscle-less humeri (as shown by the flatter collagen profiles in Fig. 4.D ii) indicate that the cartilage template is not broken down and mineralized in the same organized manner as during normal development (Ortega et al., 2004). Thus, skeletal muscles seem to promote mineralization of certain regions, while inhibiting others. This finding adds to our current understanding of the Stenciling principle (Reznikov et al., 2020), which describes how certain enzymes and inhibitors determine the location and progression of mineralization by negative regulation (inhibiting the inhibitor). In light of this principle, perhaps the presence of skeletal muscles fine-tunes the negative regulation of bone mineralization, while the lack of them results in an initially delayed, but ultimately unrestricted and unrefined mineralization.

4.4. Accelerated mineral deposition could provide an underlying mechanism for late-stage skeletal recovery in muscle-less limbs

The increased presence of Zn in the muscle-less humeri at TS27 indicates that the mineralization process has been upregulated, leading to enhanced mineralization across the rudiment. Well in line with the findings of the current study, we previously showed that the difference in mineralized size between muscle-less and control humeri is most pronounced at TS24, and that the muscle-less humeri catch up by TS27 (Pierantoni et al., 2021; Sotiriou et al., 2022). Thus, a crucial process occurs between TS24 and TS27, i.e. within only ~ 3 days, which results in an increase in mineralized volume. As the embryos grow and the free space within the uterus is reduced, passive mechanical stimuli may be exerted on the bones from movements of their mother and control littermates (Nowlan et al., 2012). The introduction of these more general forces could provide the trigger behind the accelerated mineralization towards later development stages, and its potentially more uniform stimuli could explain a more spatially homogenous mineral formation.

4.5. Limitations

The allocated time provided by synchrotrons is highly limited. Thus, the sample numbers assessed with these techniques were few and the findings should be considered as indications to guide further in-depth investigations. However, this was complemented with lab-based techniques on both structure and composition where it was possible to assess larger sample sizes. In this study, most samples were sectioned and evaluated in 2D. This provided high resolution data, enabling the possibility to observe localized patterns at the mineralization front and internal structures. However, evaluating 2D sections of 3D objects increases the impact of local variations. This limitation was partly compensated for by anralyzing the mineral particle distribution and thickness in 3D with SASTT. This novel technique clearly highlighted information that was lost in 2D and demonstrated the need for future studies to also incorporate 3D characterization techniques. SASTT involves repeated radiation, and while we found no indication of substantial effect of radiation on the mineral structural parameters that were evaluated in this study, there may have been damage on the collagen through protein disintegration as recently presented (Sauer et al., 2022). While we were able to include many complementary tissue characterization techniques, the sample preparation methods did not allow us to perform high-quality histology on the same limbs. However, the animal model is reproducible and have been extensively characterized with histology in previous studies (Nowlan et al., 2010; Pierantoni et al., 2021; Sotiriou et al., 2022; Ahmed et al., 2023). Additionally, the focus of this study was on the mineral component of the bone. However, the mineral organization and orientation are strongly linked to the

underlying collagen fibril network. Recently, Ahmed et al. (2023) showed that absence of embryonic skeletal muscles alters the localization and structure of several collagens (primarily II and X, but also I, V, VI and XI) in the developing embryonic long bone. However, the role of loading on the collagen network of the developing skeleton is still poorly understood and in need of further investigation, e.g. into the effect on fibril orientation.

5. Conclusions

This study provides new insights into how the mineralization process of long bones is affected by skeletal muscle. It highlights that a lack of skeletal muscle during prenatal bone formation could lead to a delayed but ultimately upregulated and unrefined ossification. This abnormal mineralization process could be one mechanism behind how bones in muscle-less limbs catch up in size with controls towards the end of embryonic development, but also why they still exhibit less optimized morphologies and abnormal mechanical properties. These potential key alterations due to lack of skeletal muscle provide insight into which aspects of embryonic mineralization that are in need of further investigation to improve our current understanding of the mechanisms involved during bone formation.

CRediT authorship contribution statement

Isabella Silva Barreto: Writing – original draft, Methodology, Investigation, Formal analysis. **Marianne Liebi:** Writing – review & editing, Validation, Supervision, Software, Resources, Methodology, Investigation, Formal analysis. **Sophie Le Cann:** Writing – review & editing, Methodology, Investigation, Conceptualization. **Saima Ahmed:** Writing – review & editing, Resources, Methodology. **Leonard C. Nielsen:** Writing – review & editing, Software, Resources, Methodology. **Tilman A. Grünewald:** Writing – review & editing, Resources. **Hector Dejea:** Writing – review & editing, Resources. **Viviane Lutz-Bueno:** Writing – review & editing, Resources. **Niamh C. Nowlan:** Writing – review & editing, Validation, Methodology, Funding acquisition, Conceptualization. **Hanna Isaksson:** Writing – review & editing, Validation, Supervision, Methodology, Investigation, Funding acquisition, Conceptualization.

Declaration of competing interest

The authors declare that they have no known competing financial interests or personal relationships that could have appeared to influence the work reported in this paper.

Acknowledgements

We acknowledge the Paul Scherrer Institut, Villigen, Switzerland for providing beamtime at the cSAXS beamline for the SASTT experiment under proposal 20170791. We acknowledge the European Synchrotron Radiation Facility, (ESRF) Grenoble, France for providing beamtime at the ID13 beamline for the μSAXS/WAXS/XRF experiment under proposal IH-SC-1584 and the Partnership for Soft Condensed Matter (PSCM) for support during the preparation of this experiment. We acknowledge the MAX-IV Laboratory for beamtime on the NanoMAX beamline for the nXRF experiment under proposal 20230100. Research conducted at MAX IV, a Swedish national user facility, is supported by Vetenskapsrådet (Swedish Research Council, VR) under contract 2018-07152, Vinnova (Swedish Governmental Agency for Innovation Systems) under contract 2018-04969 and Formas under contract 2019-02496. Lund University Bioimaging Centre (LBIC), Lund University, is gratefully acknowledged for providing experimental resources. We also thank Dr. Vivien Sotiriou at Imperial College London, Dr. Michiel Op de Beeck, Dr. Susanne Strömblad and Dr. Bryan Falcones Olarte at Lund University for support during the sample preparation of this study. This project received funding from the Knut and Wallenberg Foundation (KAW Grant agreement no. 2017.022), the Royal Society through a International Exchange Grant and the European Research Council under the European Union's Seventh Framework Programme (ERC Grant agreement no. 336306). M.L. and L.C.N. acknowledge funding from the European Research Council (ERC Grant agreement no. 949301) for the development of the software package MUMOTT.

Appendix A. Supplementary data

Supplementary data to this article can be found online at https://doi.org/10.1016/j.jsb.2025.108178.

Data availability

Data will be made available on request.

References

Ahmed, S., Rogers, A.V., Nowlan, N.C., 2023. Mechanical loading due to muscle movement regulates establishment of the collagen network in the developing murine skeleton. R. Soc. Open Sci. 10 (10), 231023. https://doi.org/10.1098/rsos.231023.

Balogh, E., Paragh, G., Jeney, V., 2018. Influence of iron on bone homeostasis. Pharmaceuticals. 11 (4), 1–18. https://doi.org/10.3390/ph11040107.

Boskey, A., Camacho, N.P., 2007. FT-IR imaging of native and tissue-engineered bone and cartilage. Biomaterials 28, 2465–2478. https://doi.org/10.1016/j.biomaterials.2006.11.043.

Brister, E., Vasi, Z., Antipova, O., et al., 2020. X-ray fluorescence microscopy: a method of measuring ion concentrations in the ear. Hear. Res. 391, 107948. https://doi.org/10.1016/j.heares.2020.107948.

Bromage, T.G., Goldman, H.M., McFarlin, S.C., Warshaw, J., Boyde, A., Riggs, C.M., 2003. Circularly polarized light standards for investigations of collagen fiber orientation in bone. Anat. Rec. - Part B New Anat. 274 (1), 157–168. https://doi.org/10.1002/AR.B.10031.

Buckwalter, J.A., Glimcher, M.J., Cooper, R.R., Recker, R., 1996. Bone biology. I: structure, blood supply, cells, matrix, and mineralization. Instr. Course Lect. 45, 371–386.

Bünger, M.H., Oxlund, H., Hansen, T.K., et al., 2010. Strontium and bone nanostructure in normal and ovariectomized rats investigated by scanning small-angle X-ray scattering. Calcif. Tissue Int. 86 (4), 294–306. https://doi.org/10.1007/s00223-010-9341-8.

Buss, D.J., Reznikov, N., McKee, M.D., 2020. Crossfibrillar mineral tessellation in normal and Hyp mouse bone as revealed by 3D FIB-SEM microscopy. J. Struct. Biol. 212 (2), 107603. https://doi.org/10.1016/j.jsb.2020.107603.

Casanova, E.A., Rodriguez-Palomo, A., Stähli, L., et al., 2023. SAXS imaging reveals optimized osseointegration properties of bioengineered oriented 3D-PLGA/aCaP scaffolds in a critical size bone defect model. Biomaterials 294. https://doi.org/10.1016/j.biomaterials.2022.121989 (April 2022).

Dejea, H., Raina, D.B., Silva Barreto, I., et al., 2023. Multi-scale characterization of the spatio-temporal interplay between elemental composition, mineral deposition and remodelling in bone fracture healing. Acta Biomater. 167, 135–146. https://doi.org/10.1016/j.actbio.2023.06.031.

Franz, T., Kothary, R., 1993. Characterization of the neural crest defect in Splotch (Sp1H) mutant mice using a lacZ transgene. Dev. Brain Res. 72 (1), 99–105. https://doi.org/10.1016/0165-3806(93)90163-5.

Franz, T., Kothary, R., Surani, M.A.H., Halata, Z., Grim, M., 1993. Anatomy and embryology the splotch mutation interferes with muscle development in the limbs. Vol 187.; 1993:160.

Frost, H.M., 2001. From Wolff's law to the Utah paradigm: Insights about bone physiology and its clinical applications. Anat. Rec. 262 (4), 398–419. https://doi.org/10.1002/ar.1049.

Gomez, C., David, V., Peet, N.M., et al., 2007. Absence of mechanical loading in utero influences bone mass and architecture but not innervation in Myod-Myf5-deficient mice. J. Anat. 210 (3), 259–271. https://doi.org/10.1111/j.1469-7580.2007.00698.x.

Grünewald, T.A., Liebi, M., Wittig, N.K., et al., 2020. Mapping the 3D orientation of nanocrystals and nanostructures in human bone: Indications of novel structural features. Sci. Adv. 6 (24), 4171–4183. https://doi.org/10.1126/sciadv.aba4171.

Grünewald, T.A., Johannes, A., Wittig, N.K., et al., 2023. Bone mineral properties and 3D orientation of human lamellar bone around cement lines and the Haversian system. IUCrJ. 10 (2), 189–198. https://doi.org/10.1107/s2052252523000866.

Grünewald, T., Liebi, M., Birkedal, H., 2024. Crossing length scales: X-ray approaches to studying the structure of biological materials. IUCrJ. 11:5, 708-722. doi:10.1107/S2052252524007838.

Han, C.Y., Chao, Y.F., 2006. Photoelastic modulated imaging ellipsometry by stroboscopic illumination technique. Rev. Sci. Instrum. 77 (2). https://doi.org/10.1063/1.2173027.

Kim, J.T., Baek, S.H., Lee, S.H., et al., 2009. Zinc-deficient diet decreases fetal long bone growth through decreased bone matrix formation in mice. J. Med. Food 12 (1), 118–123. https://doi.org/10.1089/jmf.2007.0647.

Liebi, M., Georgiadis, M., Menzel, A., et al., 2015. Nanostructure surveys of macroscopic specimens by small-angle scattering tensor tomography. Nature 527 (7578), 349–352. https://doi.org/10.1038/nature16056.
Liebi, M., Georgiadis, M., Kohlbrecher, J., et al., 2018. Small-angle X-ray scattering tensor tomography: Model of the three-dimensional reciprocal-space map, reconstruction algorithm and angular sampling requirements. Acta Crystallogr. Sect. Found Adv. https://doi.org/10.1107/S205327331701614X. Published Online.
Liebi, M., Lutz-Bueno, V., Guizar-Sicairos, M., et al., 2021. 3D nanoscale analysis of bone healing around degrading Mg implants evaluated by X-ray scattering tensor tomography. Acta Biomater. https://doi.org/10.1016/j.actbio.2021.07.060. Published Online.
Litchfield, T.M., Ishikawa, Y., Wu, L.N.Y., Wuthier, R.E., Sauer, G.R., 1998. Effect of metal ions on calcifying growth plate cartilage chondrocytes. Calcif. Tissue Int. 62 (4), 341–349. https://doi.org/10.1007/s002239900442.
Macías-Sánchez, E., Tarakina, N.V., Ivanov, D., Blouin, S., Berzlanovich, A.M., Fratzl, P., 2022. Spherulitic crystal growth drives mineral deposition patterns in collagen-based materials. Adv. Funct. Mater. 32 (31). https://doi.org/10.1002/adfm.202200504.
McNally, E.A., Schwarcz, H.P., Botton, G.A., Arsenault, A.L., 2012. A model for the ultrastructure of bone based on electron microscopy of ion-milled sections. PLoS One 7 (1), 1–12. https://doi.org/10.1371/journal.pone.0029258.
Micheletti, C., Shah, F.A., Palmquist, A., Grandfield, K., 2023. Ultrastructure and nanoporosity of human bone shown with correlative on-axis electron and spectroscopic tomographies. ACS Nano 17 (24), 24710–24724. https://doi.org/10.1021/acsnano.3c04633.
Mürer, F.K., Chattopadhyay, B., Madathiparambil, A.S., et al., 2021. Quantifying the hydroxyapatite orientation near the ossification front in a piglet femoral condyle using X-ray diffraction tensor tomography. Sci. Rep. 11 (1), 2144. https://doi.org/10.1038/s41598-020-80615-4.
Nichols, S., Freudenthal, J., Arteaga, O., Kahr, B., 2014. Imaging with photoelastic modulators. Polariz Meas Anal Remote Sens XI. 2014 (9099), 909912. https://doi.org/10.1117/12.2053459.
Nielsen, L.C., Erhart, P., Guizar-Sicairos, M., Liebi, M., 2023. Small-angle scattering tensor tomography algorithm for robust reconstruction of complex textures. Acta Crystallogr. Sect. Found Adv. 79 (6), 1–12. https://doi.org/10.1107/S205327332300863X.
Nielsen, L.C., Liebi, M., Erhart, P., 2023. MUMOTT software package version 0.2.https://zenodo.org/records/7919449. January 2023.
Nowlan, N.C., Murphy, P., Prendergast, P.J., 2007. Mechanobiology of embryonic limb development. Ann. N Y Acad. Sci. 1101, 389–411. https://doi.org/10.1196/annals.1389.003.
Nowlan, N.C., Sharpe, J., Roddy, K.A., Prendergast, P.J., Murphy, P., 2010. Mechanobiology of embryonic skeletal development: insights from animal models. Birth Defects Res. Part C - Embryo Today Rev. 90 (3), 203–213. https://doi.org/10.1002/bdrc.20184.
Nowlan, N.C., Dumas, G., Tajbakhsh, S., Prendergast, P.J., Murphy, P., 2012. Biophysical stimuli induced by passive movements compensate for lack of skeletal muscle during embryonic skeletogenesis. Biomech. Model Mechanobiol. https://doi.org/10.1007/s10237-011-0304-4. Published Online.
Olsen, B.R., Reginato, A.M., Wang, W., 2000. Bone development. Annu. Rev. Cell Dev. Biol. 16, 191–220. https://doi.org/10.1016/j.bone.2015.04.035.
Ortega, N., Behonick, D.J., Werb, Z., 2004. Matrix remodeling during endochondral ossification. Trends Cell Biol. 14 (2), 86–93. https://doi.org/10.1016/j.tcb.2003.12.003.
Percival, M., 1999. Bone health & osteoporosis. Appl. Nutr. Sci. Rep. 5 (4), 1–6.
Peyrin, F., 2009. Investigation of bone with synchrotron radiation imaging: from micro to nano. Osteoporos Int. 20, 1057–1063. https://doi.org/10.1007/s00198-009-0855-8.
Pierantoni, M., Le Cann, S., Sotiriou, V., et al., 2021. Muscular loading affects the 3D structure of both the mineralized rudiment and growth plate at early stages of bone formation. Bone 145 (January), 115849. https://doi.org/10.1016/j.bone.2021.115849.
Procopio, A., Malucelli, E., Pacureanu, A., et al., 2019. Chemical fingerprint of Zn–hydroxyapatite in the early stages of osteogenic differentiation. ACS Cent. Sci. 5 (8), 1449–1460. https://doi.org/10.1021/acscentsci.9b00509.
Reznikov, N., Bilton, M., Lari, L., Stevens, M.M., Kröger, R., 2018. Fractal-like hierarchical organization of bone begins at the nanoscale. Science 360, 1–10. https://doi.org/10.1126/science.aao2189.
Reznikov, N., Hoac, B., Buss, D.J., Addison, W.N., Barros, N.M.T., McKee, M.D., 2020. Biological stenciling of mineralization in the skeleton: Local enzymatic removal of inhibitors in the extracellular matrix. Bone 138 (May), 115447. https://doi.org/10.1016/j.bone.2020.115447.
Rodriguez, J.I., Garcia-Alix, A., Palacios, J., Paniagua, R., 1988. Changes in the long bones due to fetal immobility caused by neuromuscular disease. J. Bone Jt. Surg. 1052–1060. Published Online.
Roschger, P., Grabner, B.M., Rinnerthaler, S., et al., 2001. Structural development of the mineralized tissue in the human L4 vertebral body. J. Struct. Biol. 136 (2), 126–136. https://doi.org/10.1006/jsbi.2001.4427.
Sauer, K., Zizak, I., Forien, J.B., Rack, A., Scoppola, E., Zaslansky, P., 2022. Primary radiation damage in bone evolves via collagen destruction by photoelectrons and secondary emission self-absorption. Nat. Commun. 13 (1), 7829. https://doi.org/10.1038/s41467-022-34247-z.
Schamberger, B., Ehrig, S., Dechat, T., et al., 2024. Twisted-plywood-like tissue formation in vitro. Does curvature do the twist? PNAS Nexus. 3. https://doi.org/10.1093/pnasnexus/pgae121.
Schwarcz, H.P., McNally, E.A., Botton, G.A., 2014. Dark-field transmission electron microscopy of cortical bone reveals details of extrafibrillar crystals. J. Struct. Biol. 188 (3), 240–248. https://doi.org/10.1016/j.jsb.2014.10.005.
Schwarcz, H.P., Binkley, D.M., Luo, L., Grandfield, K., 2020. A search for apatite crystals in the gap zone of collagen fibrils in bone using dark-field illumination. Bone 135. https://doi.org/10.1016/j.bone.2020.115304 (December 2019).
Seidel, R., Gourrier, A., Kerschnitzki, M., et al., 2012. Synchrotron 3D SAXS analysis of bone nanostructure. Bioinspired Biomim Nanobiomaterials. 1 (2), 123–132. https://doi.org/10.1680/bbn.11.00014.
Shapiro, F., 2008. Bone development and its relation to fracture repair. the role of mesenchymal osteoblasts and surface osteoblasts. Eur. Cell. Mater. 15, 53–76. https://doi.org/10.22203/eCM.v015a05.
Sharir, A., Stern, T., Rot, C., Shahar, R., Zelzer, E., 2011. Muscle force regulates bone shaping for optimal load-bearing capacity during embryogenesis. Development 138, 3247–3259. https://doi.org/10.1242/dev.063768.
Sharma, K., Silva Barreto, I., Dejea, H., Hammerman, M., Appel, C., Geraki, K., Eliasson, P., Pierantoni, P., Isaksson, H., 2024. Elemental and Structural Characterization of Heterotopic Ossification during Achilles Tendon Healing Provides New Insights on the Formation Process. ACS Biomaterials Science & Engineering. 10:8, 4938-4946. doi:10.1021/acsbiomaterials.4c00935.
Silva Barreto, I., Le Cann, S., Ahmed, S., et al., 2020. Multiscale characterization of embryonic long bone mineralization in mice. Adv. Sci. 7 (21). https://doi.org/10.1002/advs.202002524.
Solé, V.A., Papillon, E., Cotte, M., Walter, P., Susini, J., 2007. A multiplatform code for the analysis of energy-dispersive X-ray fluorescence spectra. Spectrochim Acta - Part B at Spectrosc. 62, 63–68. https://doi.org/10.1016/j.sab.2006.12.002.
Sotiriou, V., Huang, Y., Ahmed, S., Isaksson, H., Nowlan, N.C., 2022. Prenatal murine skeletogenesis partially recovers from absent skeletal muscle as development progresses. Eur. Cell. Mater. 44, 115–132. https://doi.org/10.22203/eCM.v044a08.
Tajbakhsh, S., Rocancourt, D., Cossu, G., Buckingham, M., 1997. Redefining the genetic hierarchies controlling skeletal myogenesis: Pax-3 and Myf-5 Act upstream of MyoD. Cell 89 (1), 127–138. https://doi.org/10.1016/S0092-8674(00)80189-0.
Theiler, K., 1989. The House Mouse: Atlas of Embryonic Development. Springer-Verlag.
Turunen, M.J., Lages, S., Labrador, A., et al., 2014. Evaluation of composition and mineral structure of callus tissue in rat femoral fracture. J. Biomed. Opt. 19 (025003–1), 8. https://doi.org/10.1117/1.JBO.19.2.025003.
Ward, K.A., Caulton, J.M., Adams, J.E., Mughal, M.Z., 2006. Perspective: cerebral palsy as a model of bone development in the absence of postnatal mechanical factors. J. Musculoskelet Neuronal Interact. Published online 2006.
Wittig, N.K., Birkedal, H., 2022. Bone hierarchical structure: spatial variation across length scales. Acta Crystallogr. Sect. B: Struct. Sci. Cryst. Eng. Mater. 78, 305–311. https://doi.org/10.1107/S2052520622001524.
Wolman, M., Kasten, F.H., 1986. Polarized light microscopy in the study of the molecular structure of collagen and reticulin. Histochemistry 85 (1), 41–49. https://doi.org/10.1007/BF00508652.
Yamaguchi, M., 1998. Role of Zinc in Bone Formation and. 1998;135:119-135.